

Perspective

Transmission Electron Microscopy of Halide Perovskite Materials and Devices

Yuanyuan Zhou,^{1,*} Hadas Sternlicht,^{1,*} and Nitin P. Padture^{1,*}

Transmission electron microscopy (TEM)-based techniques are uniquely suited for site-specific structural and analytical characterization of halide perovskites (HPs) at atomic, nanometer, and micrometer length scales. TEM-based studies hold the key to understanding the nature and functionality of these fascinating materials that are at the heart of emerging solar cells and (opto)electronic devices. While TEM-based techniques have made several groundbreaking discoveries that have resulted in astonishing advancements in the field of materials science in general over the past decades, their application to HPs has been relatively sparse. Here, we provide a perspective on TEM-based studies of HPs that have been conducted so far and project a vision for how these powerful characterization techniques can be brought to bear on research problems in the field of HPs. An outlook discussing important challenges and opportunities that lay ahead is also presented.

Introduction

The field of thin-film photovoltaics (PVs) research is experiencing a revolution of sorts with the introduction of the new family of semiconducting materials—halide perovskites (HPs)—as light absorbers. The first use of HPs in solar cells was reported by Miyasaka and co-workers in 2009,¹ which has been followed by vast research activities, focusing on improving thin-film formation, materials' stability, and device architectures for more efficient and stable large-area perovskite solar cells (PSCs).^{2–6} The current record for power conversion efficiency (PCE) of single-junction PSCs has now reached 23.7%,⁷ rivalling that of commercial high-end silicon solar cells. Importantly, PSCs have the potential to be low-cost and hold great promise for their future commercialization.^{8,9} As shown in Figure 1, HPs have the general chemical formula ABX_3 , where typically A is methylammonium (MA^+), formamidinium (FA^+), or Cs^+ ; B is Pb^{2+} or Sn^{2+} ; and X is I^- , Br^- , or Cl^- . These are the most widely studied HPs for PSCs mainly because of their narrow bandgaps and favorable charge-transport properties. However, the HP family is much broader, and it also includes a number of perovskites with reduced dimensionality (2D, 1D, and 0D) or mixed dimensionality, which have proven to be superior to 3D HPs in some aspects of material properties, such as chemical stability.^{10–13} In addition, HPs can have different chemical formulas, including the well-known Ruddlesden-Popper (RP) phases, such as A_2BX_4 , ABX_4 , A_3BX_9 , etc.^{10–13} Besides the wide tunability in chemical composition, all HPs can also be processed relatively easily into nanocrystals (or quantum-dots), powders, polycrystalline thin films, and large single crystals. The nano- and micro-structural features of HPs, such as crystal defects, grain boundaries, surfaces, interfaces, and crystallographic orientations (texture), are highly tailorable as HPs are amenable to vast arrays of solution-, vapor-, and gas-based chemical processing. Therefore, HPs are a unique, yet versatile, material system that can be tuned and tailored. So far, the basic understanding of HP materials themselves is still limited, and many claimed conclusions regarding the relationships between structure and physical and chemical properties and device performance remain controversial. This is due

Context & Scale

The recent rise of halide perovskites (HPs) has revolutionized solar cells and (opto)electronic device research. Numerous studies have implied that structural and compositional characteristics of HPs at various length scales govern the device performance, but much remains poorly understood. In this context, transmission electron microscopy (TEM) has emerged as a powerful characterization tool to accelerate our fundamental understanding of HP materials and devices, with the potential of having a significant impact on the development of HP-based solar cells and (opto)electronic devices. This perspective discusses the important unsolved materials-science problems surrounding HPs and the few available examples of TEM studies of HP materials and devices in the literature. It also highlights the urgency of application of TEM-based techniques for tackling these unsolved issues. Further research in this direction is crucial for advancing the science in the increasingly important HP materials and devices field.



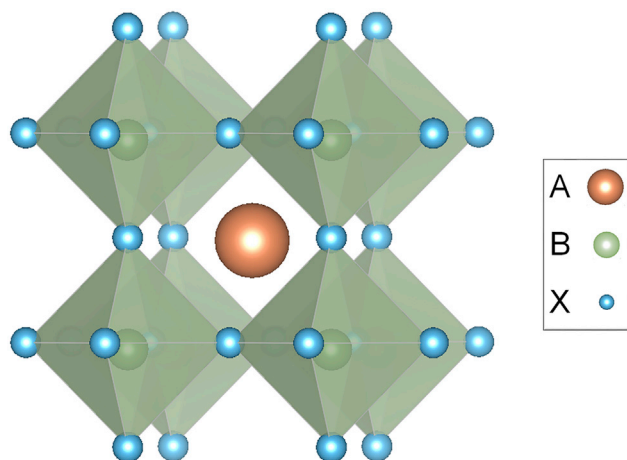


Figure 1. Schematic Representation of the ABX_3 HP Crystal Structure

to the fact that HPs have not yet been adequately characterized at the atomic to nanometer to micron length scales—the domain of TEM-based characterization, which can provide direct and deterministic insights into HP materials and devices.

Basis of TEM-Based Structural and Analytical Characterization

TEM-based characterization techniques are well established and widely used; the reader is referred to the literature cited in this section and textbooks that describe TEM basics in great detail.^{14–16} Briefly, TEM relies on interactions between an energetic electron beam and a thin electron-transparent TEM specimen of the material of interest for its characterization. Thus, the contrast that forms the TEM image depends on the specific interactions between the electron beam and the specimen.

Beyond conventional imaging of atomic resolution images, TEM offers a variety of additional imaging techniques, such as negative spherical aberration (Cs) imaging conditions^{17,18} and exit-wave reconstruction,^{19–22} which enable the contrast in a high-resolution TEM (HRTEM) micrograph to be interpreted in a relatively straightforward manner. Imaging, as well as atomic resolution imaging, can also be achieved in scanning mode (STEM), where multiple detectors such as bright field (BF), annular dark field (ADF), and high-angle annular dark field (HAADF) are used to generate the images. The resolution of an atomic resolution image, in either TEM or STEM modes, can be extended with the use of spherical (Cs) and chromatic (Cc) aberration correctors.^{23,24}

Electron diffraction patterns (EDPs) can also be generated from areas of interest in the specimen, which are used to extract crystallographic information. However, EDPs suffer from several limitations such as 2D imprecise crystallographic data due to the relaxation of Bragg conditions in thin films. Whenever an EDP does not contain sufficient information, convergent-beam electron diffraction (CBED) may be used, which enables precise crystallographic analysis of a specimen.^{14,25}

Site-specific chemical composition information can be acquired in the TEM using energy dispersive spectroscopy (EDS) and electron energy loss spectroscopy (EELS), where the latter also allows one to glean information about a variety of sample-related aspects, such as thickness, chemical surrounding, bonding, etc.^{15,26} New EDS detectors now allow high-efficiency collection of compositional data at the atomistic scale.²⁷

¹School of Engineering, Brown University, Providence, RI 02912, USA

*Correspondence:
yuanyuan_zhou@brown.edu (Y.Z.),
hadas_sternlicht@brown.edu (H.S.),
nitin_padtare@brown.edu (N.P.P.)

<https://doi.org/10.1016/j.joule.2018.12.011>

In addition to the development of improved microscope components (correctors, detectors, etc.), new specimen holders now offer the possibility of performing *in situ* experiments with minimized drift and high stability, while achieving atomic resolution.^{28–30} These holders allow imaging and collection of structural and chemical data of processes as a function of time, with the ability to heat, apply voltage, and use environments other than vacuum (liquid or gas). In specially built, dedicated environmental TEMs, instead of using special holders, the space around the specimen is designed to have variable pressure and is isolated from the rest of the high-vacuum column.³¹

While this vast array of TEM-based techniques has been successfully used to characterize a wide range of materials, beam-sensitive materials, such as HPs, cannot withstand the required currents and durations used for the acquisition of TEM data. The main beam-damage mechanisms involve heating (phonons), knock-on damage (displacement of atoms and defect formation), and radiolysis (degradation by inelastic scattering and breaking of chemical bonds).^{14,32} Several approaches can be used to overcome beam damage in beam-sensitive materials. Methods involving the illumination system include lowering the accelerating voltage and/or using low electron dosages. While beam damage depends on the accelerating voltage, the dependencies of some of the mechanisms can be countervailing. For example, lowering the accelerating voltage usually decreases knock-on damage, but it increases radiolysis. Also, low accelerating voltage results in poor resolution and shorter penetration depth. Thus, the accelerating voltage should be optimized for a given material,³³ but it does not provide a complete solution for highly beam-sensitive materials. Regardless of the selection of acceleration voltage, the use of low-dose is required when characterizing beam-sensitive materials such as HPs. The main drawback of low-dose imaging is the decrease in the signal-to-noise ratio, resulting in blurred images and missing structural information. In order to overcome this issue, stacks of short-exposure images are acquired and then aligned to eliminate drift between sequential images, forming a single final image. Also, direct detection cameras with improved detective quantum efficiency offer improved ability to separate signal from noise using lower dosages.^{34,35} In addition to the acquisition of single images, exit-wave reconstruction has been successfully performed based on a focal series acquired from beam-sensitive materials.³⁶

TEM Studies of Halide Perovskites

Atomistic and Molecular Structure

HPs are broadly divided into two categories: organic-inorganic hybrid HPs and all-inorganic HPs, depending on whether the A-site in the perovskite crystal structure is occupied by an organic-molecular cation or an elemental cation, respectively. In hybrid HPs, while the crystal structure is formed by interconnected $[BX_6]^{4-}$ octahedra extended in an ordered manner, there is local disorder within the $[BX_6]^{4-}$ framework. This is because the A-site organic cations are usually non-symmetric and tend to rotate with certain degrees of freedom at room temperature and above.³⁷ This phenomenon is unprecedented, and it has been rarely seen in other material systems. For the most-studied hybrid HP, $CH_3NH_3PbI_3$ (MAPbI₃), it has been shown that the polar MA^+ ion reorients between the faces, corners, or edges of the $[PbI_6]^{4-}$ octahedra with a residence time of ~ 14 ps at room temperature.³⁸ It has also been shown, based on the dielectric response of this material, that such rotational dynamics of MA^+ is slowed down at lower temperatures. The dynamics and polarization of MA^+ ions can also be affected by light, which could have an important effect on the physical properties and device performance of MAPbI₃ HPs.³⁹ This presents a significant challenge for direct imaging of organic cations in the TEM.

As mentioned earlier, one of the main challenges in imaging HPs using TEM is beam damage. For example, Dang et al.⁴⁰ studied transformations occurring in nanocrystals of CsPbBr₃ induced by the electron beam (200 keV) at temperatures below -40°C. In that study, it is shown that the electron beam causes decomposition, resulting in several phases, including CsBr, CsPb, and PbBr₂, and also desorption of Br from CsBr and PbBr₂. To minimize beam damage, several approaches are used. For example, Zhang et al.⁴¹ studied MAPbBr₃ utilizing low electron doses and a one-step procedure of alignment to zone axis. Their method uses the arcs that form in EDPs when the studied material deviates from the zone axis. By identifying the arc (using the position of the reflections) in a single EDP, the angle of deviation from zone axis is calculated (from the radius of the arc), such that the tilt angles in the tilt directions available in the microscope are determined. After tilting to the calculated angles, a second EDP is acquired to confirm alignment to zone axis. Using this method, they successfully oriented specimens to zone axis when the initial orientation was close to a zone axis (<5° deviation). After alignment to the zone axis, they used stacks of short-exposure images acquired using a low dose, which were then corrected for drift between successive images. The latter was accomplished using an “amplitude filter,” which enabled drift determination by “phase” variation analysis of the strong amplitude pixels in the Fourier transform (by integrating the transforms of all frames in the stack). It is suggested that this method is reliable for drift correction as a result of the minimization of the impact of noise.⁴¹ This is required due to the poor signal-to-noise ratio in single micrographs, which is inherent to low-dose acquisition, affecting the accuracy of phase determination. Calculations of the drift were performed using an iterative cross-correlations-based algorithm applied to the filtered images, before the images were summed.⁴¹ Using this approach, they observed that the MAPbBr₃ crystals contained ordered nanoscale domains with off-centered MA⁺ cations that had differing orientations (see Figure 2A).⁴¹ In Figure 2A, the MA⁺ cations exhibit configurations that are normal (region I in Figure 2A) and parallel (region II in Figure 2A) relative to the projection direction, forming in-plane and out-of-plane electric dipoles, respectively. In Figures 2B and 2C, the structural models and the corresponding simulated projected potential maps are shown. This first observation of the local variations in the MA⁺ orientation provides some evidence for the heavily discussed ferroelectricity and/or polarization in hybrid HPs in the literature.^{42–44}

While the composition of all-inorganic HPs is not as complex as that of hybrid HPs, their crystal framework is much “softer” compared with conventional oxide perovskites. Thus, there is a high possibility for local vibrations in structures, leading to changes in symmetry and structures within the crystals. Yu et al.⁴⁵ employed HRTEM, in addition to low-dose in-line holography (where Yu et al.⁴⁵ acquired a focal series in one projection),^{46,47} to visualize the pristine structure of CsPbBr₃ perovskite.⁴⁵ The CsPbBr₃ HP sample was prepared via a catalyst-free solution-phase method, and it exhibited an atomically thin 2D nanosheet morphology. Using focal series, Yu et al.⁴⁵ showed that there are two distinct phases of CsPbBr₃ (cubic and orthorhombic) HP within the nanosheets. This was confirmed using a single HRTEM micrograph acquired using a negative Cs value (Figure 2D). In Figure 2D, the two regions that are consistent with cubic and orthorhombic CsPbBr₃ phases are labeled as I and II, respectively. The difference between the cubic and orthorhombic structures was more evident in the Fourier transforms, which are in agreement with the simulated EDPs (Figures 2E and 2F, respectively). Figures 2G and 2H show enlarged images from regions I and II, respectively, overlaid with the atomic models. It is claimed that the tilting of the [PbBr₆]⁴⁻ octahedra in the orthorhombic CsPbBr₃ structure is observable using HRTEM (Figure 2H).⁴⁵ It should be noted that Kim et al.^{48,49}

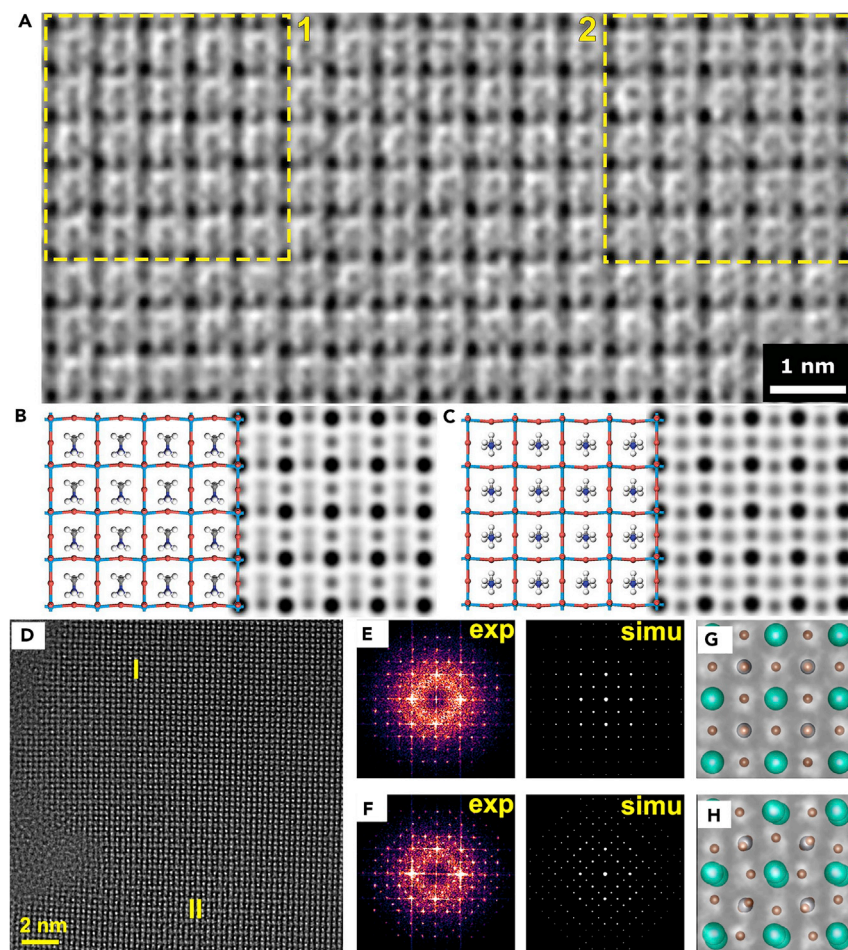


Figure 2. Atomic-Resolution TEM Images of HPs

(A) The squares highlight two ordered domains with off-centered MA^+ cations in MAPbBr_3 that have different orientations.

(B and C) Structural models (left) and the simulated projected potential maps (right) of MAPbBr_3 with MA^+ orientations (B) normal and (C) parallel relative to the projection direction corresponding to regions 1 and 2 in (A), respectively.

(A–C) Adapted from Zhang et al.⁴¹ with permission, the American Association for the Advancement of Science.

(D) HRTEM image acquired using a negative C_s value of CsPbBr_3 showing coexistence of cubic (region I) and orthorhombic (region II) structures within a nanosheet.

(E and F) Experimental Fourier transforms and the corresponding simulated EDPs of cubic (E) and orthorhombic (F) CsPbBr_3 , respectively.

(G and H) Enlarged images of regions I and II overlaid with the cubic (G) and orthorhombic (H) CsPbBr_3 structure models, respectively.

(D–H) Adapted from Yu et al.⁴⁵ with permission, the American Chemical Society.

have also observed the coexistence of several phases in HPs, where they suggested the presence of the cubic and tetragonal phases in MAPbI_3 , whereas in an earlier study, Dar et al.⁵⁰ reported the observation of tetragonal phase in MAPbI_3 . Reis et al.⁵¹ have used CBED to determine the space group and to estimate the octahedral rotations of CsPbBr_3 using low-dose to extract 4D STEM datasets, where the tetragonal phase was detected at cryogenic temperature.

RP HP phases, with the chemical formula $\text{A}_{n+1}\text{B}_n\text{X}_{3n+1}$, where A and B are cations and X is a halogen (sometimes represented as $\text{A}'_2\text{A}_{n-1}\text{B}_n\text{X}_{3n+1}$, where A' is a second

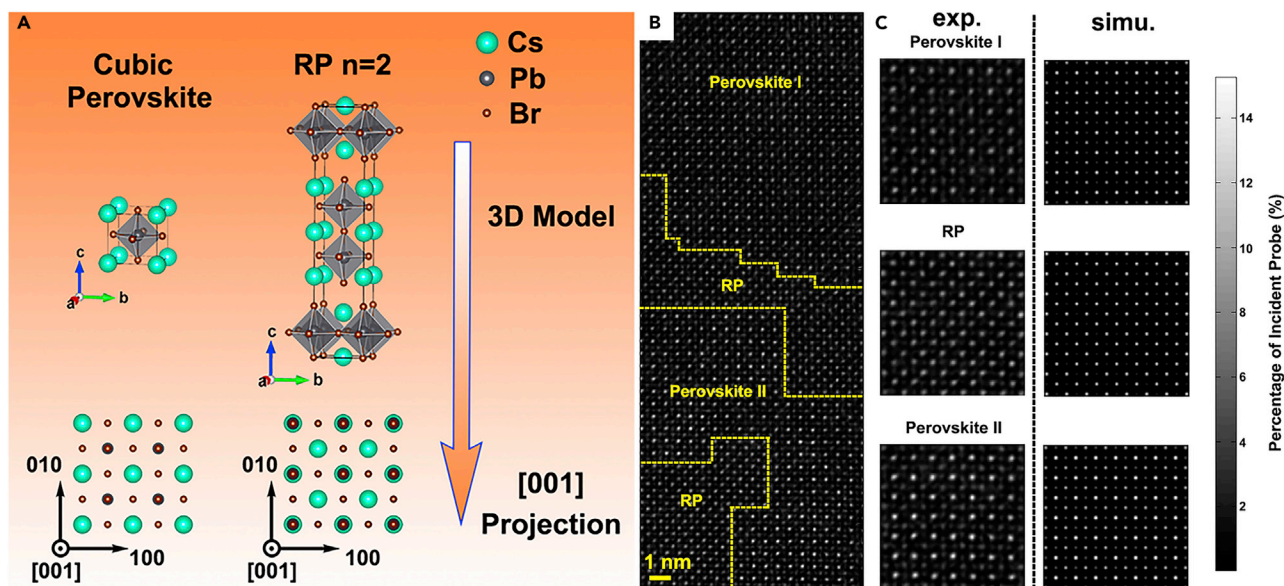


Figure 3. Coexistence of Different Phases in an HP

(A) Schematic representation of the crystal structures of the cubic CsPbBr_3 perovskite phase and one of the corresponding RP phases, $\text{Cs}_{n+1}\text{Pb}_n\text{Br}_{3n+1}$, for which $n = 2$, in addition to the corresponding projections along the $[001]$ zone axis (bottom).

(B) HAADF STEM image showing the coexistence of RP and perovskite phases of CsPbBr_3 HP.

(C) Comparison between experimental and simulated images. The left column is the enlarged images from different areas marked in (B), and the right column is the corresponding simulated images. Adapted from Yu et al.⁵³ with permission, the American Chemical Society.

A-site cation) have attracted attention for their use in PSCs and light emitting diodes (LEDs), owing to their chemical stability and bulk quantum effects compared to other HPs.⁵² However, hybrid or all-inorganic RP HPs have rarely been characterized at the nanoscale. Thus, the mechanisms underlying the high-performance and high stability in RP HP-based devices are poorly understood. In contrast, previous TEM studies on RP phases of oxide perovskites have been very successful. The main STEM study involving RP HPs is by Yu et al.,⁵³ where in CsPbBr_3 nanosheets (which were found to be cubic or orthorhombic, as discussed above), they observed deviation from the expected STEM contrast of the CsPbBr_3 phase. While for CsPbBr_3 in the $[001]$ zone axis, the contrast of Pb-Br and Cs columns of atoms varied due to the Z-contrast in HAADF STEM images (heavier Pb-Br columns showed the highest brightness, and the lighter Cs columns showed weaker brightness), and it was found that there were areas in which both columns of atoms appeared as high-bright contrast. This agrees with the RP structure of CsPbBr_3 , which can be described as $\text{Cs}_{n+1}\text{Pb}_n\text{Br}_{3n+1}$. The structure of these phases includes an in-plane shift between two adjacent CsPbBr_3 units, resulting in the formation of mixed Cs-Pb-Br columns of atoms in the $[001]$ zone axis, which appear in bright contrast in HAADF STEM, deviating from the contrast of CsPbBr_3 . In Figure 3A, the schematic illustrations of the 3D structure models, as well as the $[001]$ projections of both the cubic CsPbBr_3 HP phase and the RP HP phase (for $n = 2$), are shown. Yu et al.⁵³ found that the perovskite and the RP phases coexist in single nanosheets (Figure 3B). Figure 3C shows enlarged HAADF STEM images from the regions labeled perovskite I and II, and RP in Figure 3B, and their corresponding simulated images (performed using the multislice method^{14,54,55}). It is claimed that the difference between the regions labeled perovskite I and II was the termination of the surface.⁵³

It should be taken into account that structural and compositional changes are expected to occur during TEM characterization of HPs due to the interaction with

the electron beam (beam damage). For example, several phase transitions were demonstrated in the study by Rothmann et al.⁵⁶ In that study it was shown that even under certain low dose conditions the EDP of MAPbI₃ changed as a function of time and dose, where the tetragonal phase was initially detected. These changes included the appearance of reflection forbidden for the tetragonal phase, variations in the intensity of reflections, and a decrease in the *d*-spacing as a function of time.⁵⁶ While this was demonstrated for MAPbI₃,⁵⁶ phase transitions as a result of beam damage are expected to occur in beam-sensitive materials in general (depending on the dose). As such, beam damage might explain the presence of multiple phases in the data reported in the literature. The possible coexistence of several phases may also be affected by the material preparation method, and we envision that manipulation of the phases by altering processing conditions may be a new way to improve the charge transport and chemical stability of HPs.

Nano- and Micro-structures in Halide Perovskites

The influence of nano- and micro-structures, such as grain size and grain boundaries, on material properties and devices have been widely studied in the field of materials science. While nano- and micro-structure can be addressed using characterization techniques such as scanning electron microscopy (SEM) and atomic force microscopy (AFM), TEM can contribute to in-depth characterization.

A key to understanding the nano- and micro-structure of materials is to reveal the elemental distribution at the nanoscale, which is particularly important for HPs. The best-performing HPs are usually not of the simple ABX₃ composition, and typically contain multiple cations and/or anions, forming mixed-composition HPs. Such mixed-composition HPs can be easily prepared using iso- and alio-valent doping or alloying by controlling the precursor compositions or by post-deposition chemical incorporation. For example, the state-of-the-art HPs that are used in high-efficiency PSCs are in the system (Rb,Cs,MA,FA)Pb(I,Br)₃. While the chemical formulas of these HPs are usually adopted from the molar ratios of ions in the precursor solutions, the exact phase compositions in such complex systems could vary from what is expected, and most likely include several phases. For example, in Cs-, Rb-, and K-incorporated hybrid organic-inorganic HPs, the polar organic cation and non-polar inorganic cations are mixed, and second phases may appear at grain boundaries. Such phases cannot be fully characterized using X-ray diffraction (XRD) or SEM techniques due to the small amount of highly dispersed Cs, Rb, and K. In such cases, TEM characterization is indispensable. For example, Xiao et al.⁵⁷ have studied MAPb(I_{0.6}Br_{0.4})₃, Cs_{0.6}MA_{0.4}Pb(I_{0.6}Br_{0.4})₃, and BA_{0.6}Br_{0.4}-Cs_{0.6}MA_{0.4}Pb(I_{0.6}Br_{0.4})₃ (where BA is n-butylammonium, and BA_{0.6}Br_{0.4} acts as a capping layer used to prevent halide migration). In that work, it was shown that the films are polycrystalline with a grain size of few tens of nanometers. It is suggested that in Cs_{0.6}MA_{0.4}Pb(I_{0.6}Br_{0.4})₃ and BA_{0.6}Br_{0.4}-Cs_{0.6}MA_{0.4}Pb(I_{0.6}Br_{0.4})₃ films, the composition is uniform after illumination, whereas in MAPb(I_{0.6}Br_{0.4})₃ the halides redistributed after illumination.⁵⁷ In another TEM study, Bekenstein et al.⁵⁸ investigated Cs₂AgBiBr₆ and Cs₂AgBiCl₆, where it is suggested that Ag grains form during degradation of the films, based on EDS maps as well as HAADF STEM and HRTEM imaging.

HP thin films used in PSCs and (opto)electronic devices are invariably polycrystalline, and thus, grain boundaries are ubiquitous. While there is an ongoing debate about the importance of the role of grain boundaries in HPs, it is becoming increasingly clear that grain boundaries can serve as recombination sites, restrict photocarriers, and serve as "highways" for the undesirable transport of ionic and molecular species. Grain boundaries are characterized by five macroscopic degrees of freedom:

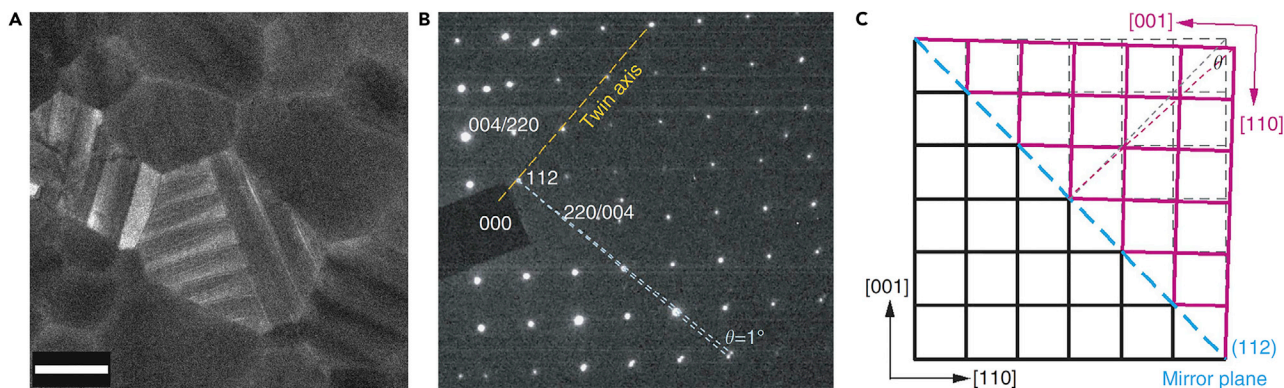


Figure 4. Twinning in MAPbI₃ HP

(A) TEM image of twin boundaries in a MAPbI₃ thin film at room temperature. Scale bar is 500 nm.

(B) SAEDP showing twinning.

(C) Schematic representation showing the proposed twinning geometry in the [110] oriented tetragonal MAPbI₃ lattice. The original lattice without twinning is depicted by thin dashed lines. Adapted from Rothmann et al.⁶² with permission, the Nature Publishing Group.

three to describe the misorientation between the adjacent grains and two to describe the boundary plane itself.^{59,60} TEM can be used to characterize these parameters. In this context, a special type of grain boundary is a twin boundary, where there is a high-symmetry relation between the delimiting grains. Twin boundaries in materials can form during growth, phase transition, or under mechanical stress. For example, twin boundaries in CdTe have been characterized extensively and found to play an important role on the PV performance.⁶¹ For hard materials such as CdTe, twin boundaries may become observable by chemical etching,⁶¹ but for HPs, due to their extreme sensitivity to chemical solvents and solutions, chemical etching is not a feasible way for observing twin boundaries. Thus, TEM and electron back-scattered diffraction (EBSD) are essential tools for revealing twinning in HPs. In this context, Rothmann et al.⁶² studied twin boundaries in the MAPbI₃ HP using TEM. Based on low-dose TEM imaging and selected area EDPs (SAEDPs), they showed the presence of twinning in tetragonal MAPbI₃, where these boundaries appeared in the form of parallel stripes within MAPbI₃ grains, forming bands that were a few hundred nanometers in width (Figure 4A). The SAEDPs of these twins showed slight rotation of the diffraction spots of each grain, where the rotation was most pronounced for high-index reflections (Figure 4B). The twin axis was found to pass through (*h h 2h*) reflections and is marked in Figure 4B, resulting in a mirror plane parallel to {112} planes of tetragonal MAPbI₃. Figure 4C presents a schematic representation of the proposed twinning geometry. The twin boundaries disappeared upon *in situ* heating to 70°C and phase transformation to the cubic phase.⁶² Upon cooling, the twins reappeared, thus indicating that their presence is inherent to the tetragonal phase and that they form reversibly upon the cubic-to-tetragonal phase transformation.⁶² The effect of such twins on HP properties and device performance is not clear. However, a recent study has shown that special boundaries such as twins can be very effective in restricting photocarriers.⁶³ Thus, manipulating the characteristics of twinning (size, orientations, etc.) could be a viable approach for the attainment and tailoring of new properties in HPs.

Grain boundaries can have different chemistries compared to the bulk grains due to segregation and/or the formation of second phases (wetting or partially wetting) along grain boundaries. In this context, TEM is uniquely suited to analyze site-specific grain-boundary chemistry. In PSCs, grain-boundary chemistry is of vital importance because it strongly affects carrier recombination and potential transport

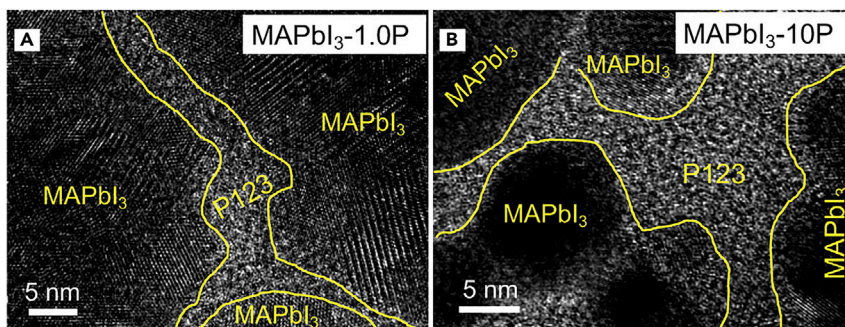


Figure 5. Chemical Functionalization of Grain Boundaries in MAPbI₃ HP Thin Films

(A and B) TEM images of thin films where (A) 1 wt% and (B) 10 wt% triblock copolymer Pluronic P123 were added to the precursor solution. Adapted from Zong et al.⁶⁴ with permission, Cell Press.

of ionic and molecular species, thus influencing the overall optoelectronic properties and chemical stability of HPs. The grain-boundary chemistry of HPs can be dependent on the HP bulk composition, the processing conditions, the structure of the boundary, the kinetic state of the boundary, as well as on deliberate chemical modifications. Thus, understanding the grain-boundary chemistry is a prerequisite for performing grain-boundary engineering for improved HPs and PSCs. In a recent study,⁶⁴ MAPbI₃ HP grain boundaries were functionalized by triblock copolymer (Pluronic P123) resulting in water-resistant HPs. Figure 5 presents phase boundaries between amorphous wetting films of copolymer and MAPbI₃ grains. It was assumed that the copolymer interacted with HP grains via its hydrophilic tails, leaving its hydrophobic core in the center of the copolymer wetting film thus, resulting in an HP that is resistant to water from the environment.⁶⁴ This strategy has significantly improved the stability of the HP films, benefiting from grain-boundary engineering supported by TEM characterization. Future TEM studies in this direction, such as studying the nature of the bonding between HPs and copolymers, will provide useful information for designing advanced polymer structures to tune the HP properties through grain-boundary functionalization.

It is important to note that variations in the nano- and micro-structure of HPs is also expected to occur due to beam damage upon TEM characterization (depending on the dose), as it is also reported in the literature. As mentioned earlier, Rothmann et al.⁵⁶ have shown that structural and compositional changes occur in MAPbI₃ as a function of time and dose, due to the interaction of MAPbI₃ with the electron beam. In that study, it was also shown that the twin boundaries inherent to the tetragonal phase (as shown in Rothmann et al.⁶²) disappeared upon TEM characterization and structural and compositional changes, even under low dose conditions. Finally, cracking of the films was noted upon several minutes of TEM characterization, and it was correlated to the structural and compositional changes that were reported.⁵⁶ Thus, there is a crucial need to address alterations of the nano- and micro-structure of the specimens due to beam damage.

HP Structures and Interfaces in Devices

The microstructure of HP thin films in PSC devices depends on the device architecture, which is broadly divided into two types: planar and mesoscopic PSCs.⁶⁵ In planar devices, the HP thin films (300–400 nm thick) are sandwiched between a flat anode and a cathode, while in mesoscopic devices, typically a mesoporous (~20 nm pore size) TiO₂ layer (200–500 nm) is incorporated on the anode side,

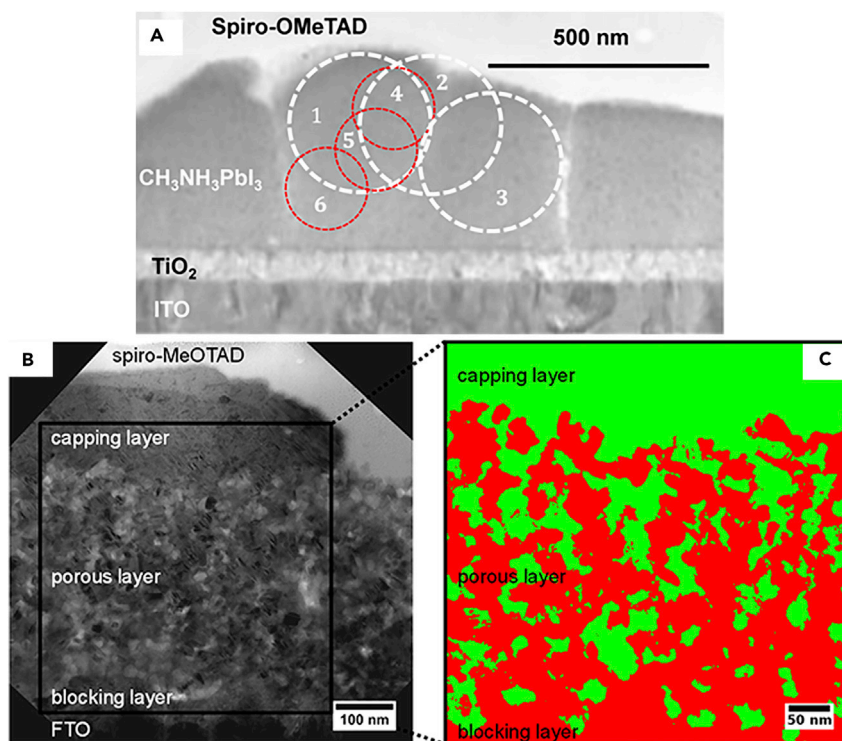


Figure 6. Micro-structure of HP Devices

(A) Cross-sectional bright-field TEM image showing the morphology of HP in a planar PSC device. SAEDPs were obtained from the areas marked by circles, confirming that areas marked as 1,4,5,6 were taken from one grain, 3 was taken from an adjacent grain and 2 from the boundary between the two grains. Adapted with permission from Yang et al.⁶⁶, the American Chemical Society.

(B) A zero-loss filtered image of the studied cell.

(C) False-color map of the TiO₂ (in red) and perovskite-rich areas (in green) based on statistical analysis of ESI series. (B)-(C) Adapted from Nanova et al.⁶⁸ with permission, the American Chemical Society.

and the HP material is infiltrated into the mesopores.⁶⁵ However, the highest performing PSCs combine the two types where a dense HP “capping” layer is included on top of a thinner mesoscopic layer. While planar PSCs are simple and easier to process, the insertion of the mesoscopic layer consisting of an interpenetrating TiO₂-HP nanocomposite of optimized thickness has been found to improve charge-injection, light absorption, film morphology, HP stability, and mechanical adhesion.

In planar PSCs, the HP thin film is typically polycrystalline, with an average grain size ranging from tens of nanometers to a few microns. A large grain size is desirable, with grains spanning the entire thickness of the film. Not surprisingly, the highest PCEs obtained in planar PSCs have been with HP thin films of grain size well above the film thickness, where there is a low density of only “vertical” grain boundaries. Figure 6A presents such vertical grain boundaries in a study by Yang et al.⁶⁶ The orientation and increased size of the HP grains were confirmed using SAEDPs from multiple areas in Figure 6A. As a result of the presence of other device layers in contact with the HP layer, there can be interactions between those layers creating complex interfaces. Yang et al.⁶⁶ have characterized such interfaces using STEM and EELS, and they have suggested that HP grain boundaries are infiltrated by the spiro-OMeTAD hole-transporting layer (HTL) material. Such grain boundaries in devices are claimed to be responsible for the near-100% internal quantum efficiency in their

PSCs. In another study, it has been claimed that in a planar PSCs with inverted-architecture, the phenyl-C61-butyric acid methyl ester (PCBM) molecules from the electron-transporting layer (ETL) material can infiltrate into HP grain boundaries after solution processing, which can reduce the photocurrent hysteresis of the devices, but that is yet to be confirmed using TEM.⁶⁷

In mesoscopic PSCs, the complex nature of the nanostructure HP thin films makes it more complicated to characterize them. This is particularly true for doped or alloyed HPs with mixed-compositions. Variations in composition and nanostructure in devices are expected, and analytical TEM is ideally suited for their characterization, correlating them back to the performance of the HP devices. Nanova et al.⁶⁸ reported a comprehensive TEM study of mesoscopic PSCs. The HP layer in their study was prepared using chlorine-containing recipe of MAI + PbCl₂ (3:1 molar ratio) in dimethylformamide (DMF), where cross-section TEM specimens of PSCs were prepared using focused ion beam (FIB). Figure 6B shows a zero-loss filtered image of the studied cell. Figure 6C is a false-color map of the phases in the system based on statistical analysis of electron spectroscopy imaging (ESI) series from the area indicated in Figure 6B showing two types of regions: HP-rich (in green) and TiO₂-rich (in red).^{68,69} In this approach, while overlap between the two phases is expected (as the size of the areas containing each phase may be smaller than the thickness of the specimen), the classification of materials was performed according to the highest relative contribution of the two materials, and as a result, it does not represent pure materials. The ESI map shows a highly interconnected TiO₂ network with 10–80 nm size mesopores that are fully and continuously infiltrated by HP. In another study, Zhou et al.⁶⁵ characterized HPs in mesoscopic TiO₂ scaffold in plan and cross-sectional views. In a plan-view specimen, the mesoporous TiO₂ and HP layers were successively deposited on a TEM grid. In that study, it was suggested that nanoscale MAPbI₃ HP grains are present within the TiO₂ mesopores, and larger MAPbI₃ grains are present in the capping layer. The difference in the grain size of MAPbI₃ in the mesopores and capping layers may affect the properties of PSCs, which awaits further investigation. As these TEM studies were conducted on relative simple HP systems, future research of these systems (such as segregation at the TiO₂-HP interface) will assist in gaining control over the HP nanostructure and composition distributions in mesoscopic PSC devices.

Finally, it should be taken into account that chemical, structural, and nano- and micro-structural changes occur upon TEM characterization due to the sensitivity of HPs to the electron beam (see for example Zhang et al.⁴¹ and Rothmann et al.⁵⁶) in addition to beam damage during FIB sample preparation. As such, there is a crucial need to eliminate alterations resulting from beam damage, which so far are not always addressed in the literature. Beam damage becomes even more important when dealing with interfaces due to their enhanced sensitivity (see Rothmann et al.⁵⁶) and the high doses usually required for “conventional” EELS and EDS acquisition used for their compositional characterization.

In Situ TEM Studies

Crystallization and Grain Size

HP thin films in PSCs are typically deposited using solution processing involving relatively low temperatures.⁷⁰ In most cases, the precursor compounds are dissolved in polar solvents, and the solution is spread thin using a variety of methods, with spin-coating being the most popular. There are two main types of HPs crystallization mechanisms from solutions. The first is direct nucleation and grain growth of HP crystals from supersaturated precursor solutions. In this case, the HP nucleates by

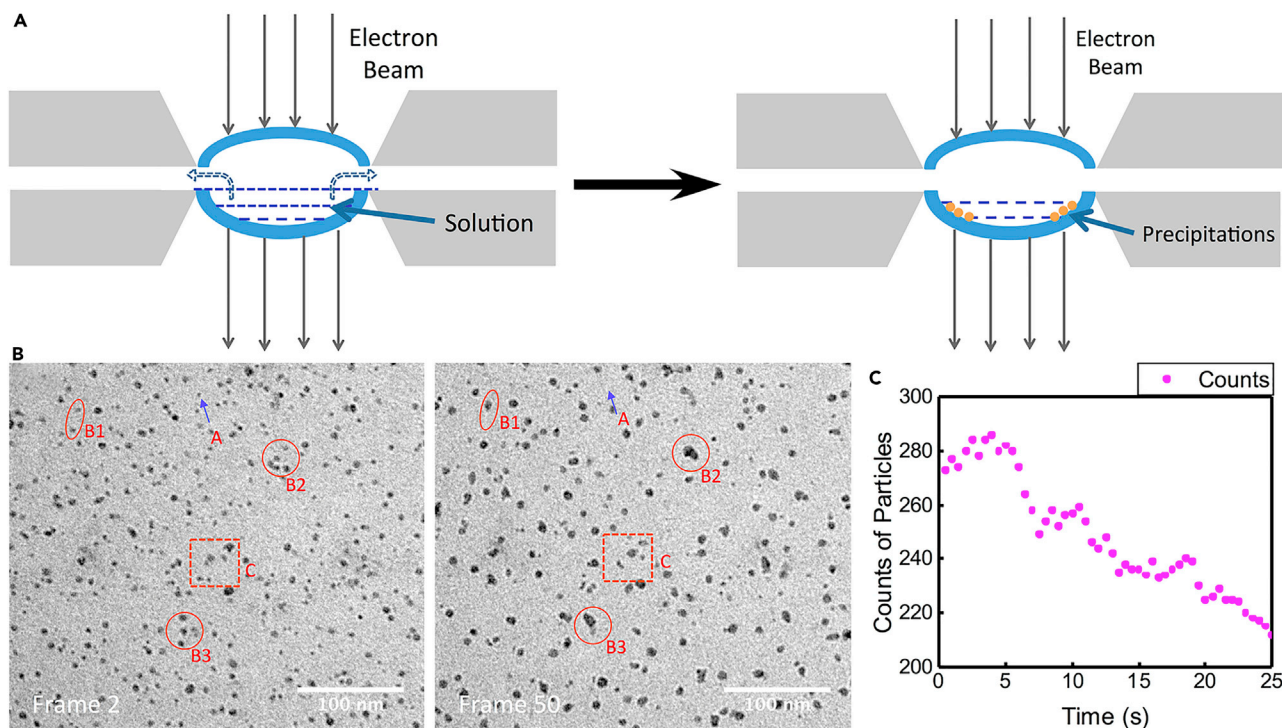


Figure 7. Crystallization of MAPbI₃ HP from Solution

(A) Schematic representation of the precipitation process of MAPbI₃ perovskite via solvent evaporation promoted by the electron beam.

(B) TEM images showing the aggregation and coalescence of MAPbI₃ nanoparticles. Arrow A marks shrinking or disappearing nanoparticle, and circles B1–B3 indicate the aggregation or coalescence of nanoparticles. Square C was used to follow the dynamic behavior of the nanoparticles indicating Brownian-type motion.

(C) The number of nanoparticles as a function of time.

Adapted from Qi et al.⁷² with permission, the American Chemical Society.

heterogeneous or homogenous nucleation, followed by growth of the stable nuclei into larger grains, which eventually forms the thin film. The second mechanism, which is more common for HPs, is the adduct-mediated crystallization.⁷¹ In this case, the initially crystallized phase from the HP precursor solution is not HP, and instead an intermediate solvated-perovskite complex—an adduct—forms, which subsequently transforms to HP upon the removal of solvent molecules by moderate heating. This is commonly observed because the polar solvents that are used for preparing the HP precursor solutions coordinate strongly with HPs, especially Pb-based HPs. Typically, the intermediate phase converts to phase-pure HP through several steps, where the morphology of the intermediate phases may be preserved or transformed based on the nature of the conversion reactions. While enormous amount of research has been performed in this direction, it is primarily intuitive and heuristic in nature, and the exact mechanisms of such processes are not yet fully understood. Understanding the detailed crystallization and growth processes of HPs will provide useful scientific guidance for exploring reliable deposition methods for HP thin films and opportunities to make better-quality films. Since the processes involved in the formation of HP thin films from solutions occur at the molecular and nanometers length scales, *in situ* TEM techniques are uniquely suited for elucidating the detailed mechanisms by which these processes take place.

In this context, Qin et al.⁷² have used an *in situ* liquid-cell for studying the crystallization of MAPbI₃ HP from its solution in DMF solvent. Figure 7A presents

schematic illustrations of the *in situ* TEM study for observing the precipitation of MAPbI₃ HPs from solution, where the supersaturation of the solution was promoted by the electron beam.⁷² Figure 7B shows TEM images that capture the change over time, indicating aggregation or coalescence of MAPbI₃ precipitates. This caused a decrease in the number of nanoparticles as a function of time as shown in Figure 7C, where the motion of the nanoparticles was found to be Brownian-like.⁷² In another *in situ* TEM study, Augiar et al.⁷³ used a gas-cell to investigate the evolution of FAPbI₃ HP from an adduct during heating. Using STEM and EELS, it was suggested that the Pb redistributed during HP crystallization as the temperature was increased. Because of changes in the Pb EELS edge between the Pb detected inside the grains and at the grain boundaries, it was suggested that the bonding of Pb varies.⁷³ It should be considered that, as discussed in the previous section for *ex situ* characterization, beam damage during TEM characterization might alter the composition, structure, and nano- and micro-structure of HPs. Thus, there is a need to eliminate and access variations in the characterized samples that result from the characterization process itself due to beam damage, which is so far lacking in the reported literature.

Thermal and Environmental Degradation of Halide Perovskites

HPs, especially hybrid HPs, are susceptible to chemical degradation upon thermal heating and atmospheric (O₂, H₂O, solvent-vapor, etc.) exposure, where the HP microstructures play a significant role. Numerous studies have shown that HP single crystals are thermally more stable compared to HP polycrystalline thin films, implying that grain boundaries most likely provide pathways for degradation, resulting in low stability.^{74,75}

Regarding thermal degradation, Kim et al.⁷⁶ have performed an *in situ* TEM study on MAPbI₃ HP grains, indicating that the degradation product is PbI₂. It is further suggested that PbI₂ crystallizes from amorphous regions of MPbI₃ via a series of intermediate states.⁷⁶ This is in agreement with the work by Chen et al.,⁷⁷ who studied the degradation of MAPbI₃ under electron-beam irradiation and observed the formation of hexagonal PbI₂, where the decomposition process is suggested to include the loss of iodine ions. Environmental degradation of HPs induced by H₂O and O₂ in air is more complex and potentially involves chemical processes including hydration, decomposition, phase transition, and oxidation, where the exact mechanisms or pathways of HP degradation are highly dependent on the HP composition. For example, in the *in situ* TEM experiments performed by Augiar et al.,⁷⁸ where FAPbI₃ HP in Ar containing 10 mbar of H₂O was heated, formation of voids at grain boundaries was observed, in addition to an increase in grain size at elevated temperatures. In the absence of water vapor, under the same heating conditions, no noticeable voids were observed.⁷⁸ As such, the appearance of voids was correlated to the presence of water pressure. To mimic ambient air, *in situ* TEM experiments were conducted using FAPbI₃ HP specimens in atmosphere containing water vapor mixed with O₂+N₂.⁷⁸ In this case, larger grains were detected, in addition to a smaller number of voids, compared to the case without the O₂+N₂. These observations indicate that humidity during processing affects the morphology of the FAPbI₃.

Fan et al.⁷⁹ have also studied thermal degradation of MAPbI₃ HP using low dose *in situ* TEM, suggesting that at 85°C, under vacuum or dry air, the films showed a gradual evolution from tetragonal MAPbI₃ to trigonal PbI₂. Previously, moisture-induced degradation of MAPbI₃ is suggested to originate with hydration of water molecules of HP crystals, forming MAPbI₃·xH₂O, which further decomposed to

PbI_2 , MAI, and H_2O .^{79,80} In addition, Wang et al.⁷⁴ have claimed that H_2O molecules ingress preferentially into the MAPbI_3 HP thin film through grain boundaries.

Dang et al.⁸¹ have studied beam damage in the presence and absence of heating in orthorhombic CsPbBr_3 . It is suggested that radiolysis was more pronounced than knock-on damage as larger compositional changes induced by the beam were detected at 80 keV rather than at 200 keV.⁸¹ These compositional changes included a decrease in the amount of Br, which was detected, as well as the formation of Pb nanoparticles (with face-centered cubic structure). In addition, it is suggested that no significant temperature rise took place, as there was a lack of significant changes in the size of Pb particles at different electron-beam irradiation conditions. Upon heating (from -20°C to room temperature) with and without irradiation, larger Pb nanoparticles formed. Pb particles were largest upon combined heating and irradiation.⁸¹ It should be taken into account that radiolysis is also claimed to be the main beam-damage mechanism in CsPbI_3 .⁸²

Considering the metastability of HPs and many HP-related compounds (HP hydrates, etc.), many unexpected phenomena may occur during the degradation of HPs, which could play an important role in the degradation of HP devices. Although several of the HP degradation mechanisms are not yet clear, the past heuristic efforts and achievements toward enhancing the thermal and atmospheric stability of HPs have been notably outstanding. In addition, incorporation of Cs, Rb, K, and large organic cations into HPs, forming mixed-composition HPs, has been found to enhance the stability to a large extent.^{9,83,84} However, the stability of HPs is still far from meeting the requirements for real-world applications, for which effective compositional-engineering protocols need to be developed for HP stabilization.

It should be considered that beam damage during TEM characterization also leads to degradation of HPs (see for example Zhang et al.⁴¹ and Rothmann et al.⁵⁶). Thus, in the case of thermal/environmental degradation of HPs, the need to address beam damage alterations to the samples apart from degradation resulting from heat and the environment is critical. While beam damage was partly addressed for *ex situ* characterization of HPs in very few cases,⁵⁶ beam damage characterization and its minimization (or preferably elimination) during *in situ* experiments is also lacking.

Degradation of Halide Perovskite Devices

HP degradation in devices is a more complex problem than the degradation of HP materials themselves, as it involves the interaction of HPs with species from other layers in the devices. For a typical PSC with a transparent conducting oxide (TCO)/ TiO_2 anode and a spiro-OMeTAD/Au cathode, the HP degradation may be caused by diffusion of components of the spiro-OMeTAD layer into the HPs, Au diffusion into HPs, or interfacial chemical reactions of HPs with other layers. For example, using EELS and HAADF STEM, Yang et al.⁸⁵ claim that Pb-rich particles form in air-exposed samples of TCO/ TiO_2 / MAPbI_3 /spiro-OMeTAD/Ag devices. Using *in situ* TEM (where the specimen was stored in the microscope with the beam blanked, and HAADF STEM micrographs were acquired on a daily basis), it is observed that minimal degradation occurs under vacuum after prolonged durations. However, upon heating to 50 – 60°C in a H_2O - and O_2 -free environment further degradation of HP layer was detected.

Divitini et al.⁸⁶ have studied the thermally induced degradation in a PSC device using *in situ* TEM. Figure 8A shows elemental migration in PSC upon heating, where the HP layer was found to degrade and small PbI_2 particles formed, in addition to

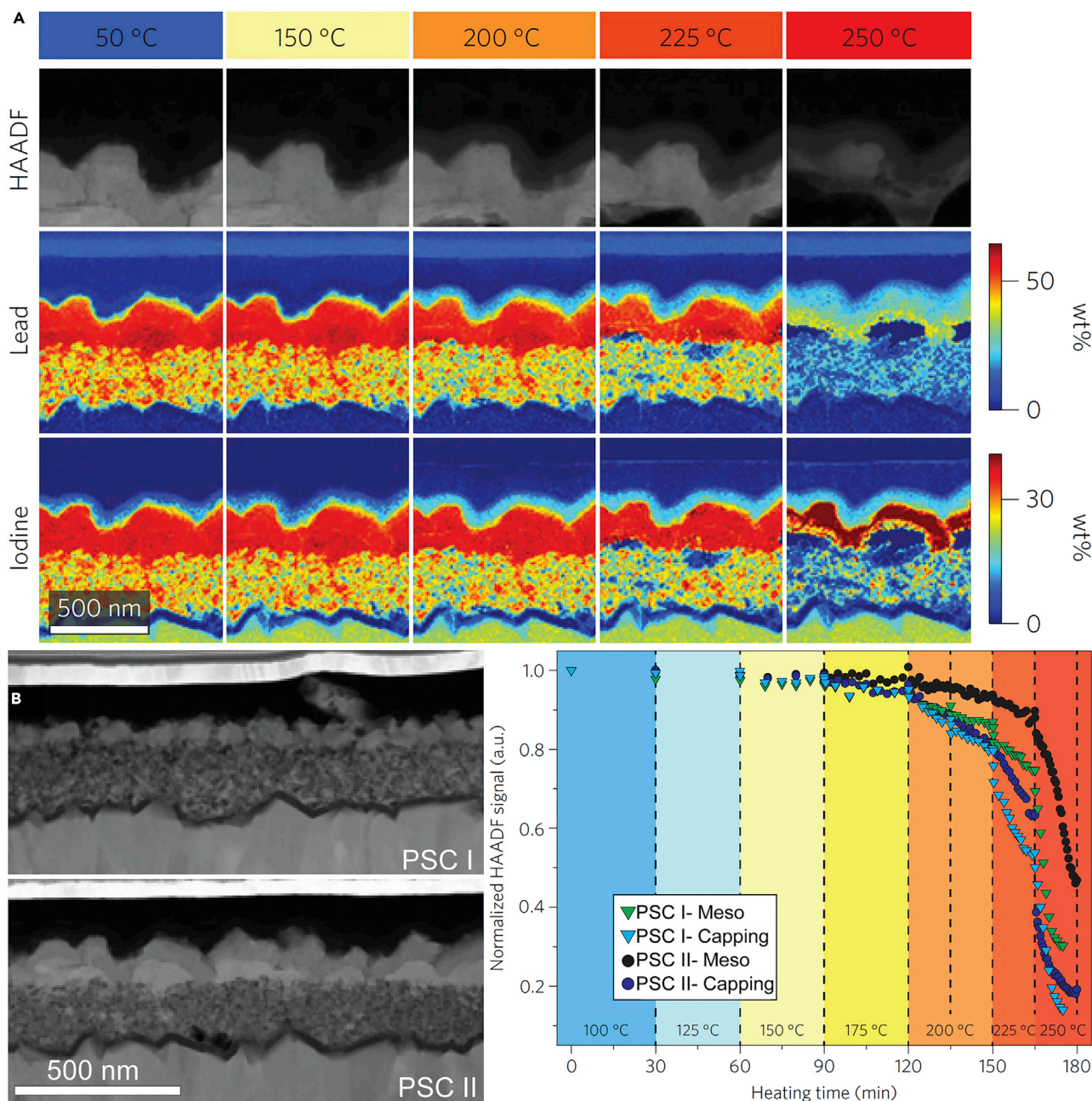


Figure 8. Thermal and Environmental Degradation of PSCs

(A) HAADF STEM images and EDS elemental maps of iodine and lead for a MAPbI₃ PSC (prepared using a two-step method in 50% relative humidity air) after heating at different temperatures. Same scale bar applies for all images.

(B) Variation of the STEM HAADF signal during the heating ramps for two different PSC samples averaged over the entire film for both the mesoporous and capping layers (PSC-I: HP layer processed in dry N₂; PSC-II: HP layer processed in 50% relative humidity air). Images were acquired at 50°C. Same scale bar applies for both images. Adapted from Divitini et al.⁸⁶ with permission, the Nature Publishing Group.

the formation of holes, mainly in the HP layer next to the TiO₂ scaffold. Figure 8A indicates that diffusion of iodine into the spiro-OMeTAD layer started first at low temperatures, and Pb diffusion was triggered only at higher temperatures. Divitini et al.⁸⁶ further plotted the profiles of the HAADF STEM signal of the devices (Figure 8B) to obtain a quantitative estimate of the device degradation along time.

Two different PSCs, PSC-I (HP layer processed in dry N_2) and PSC-II (HP layer processed in air), were compared. As seen in Figure 8B, very little variations appear before 150°C, followed by a fast decay. The intensity-decay appeared much slower in the mesoporous layers than in the capping layers, indicative of a higher stability for the HP in mesopores. In addition, the signal decay in PSC-II was slower than that in PSC-I, which is unexpected as PSC-II was processed in humid air. It is proposed that small amounts of oxygen and water that were incorporated in the HP layer may have retarded ion diffusion.⁸⁶ While many new concepts of device design have been proposed in order to overcome degradation issues in devices, TEM studies are helpful for identifying device stabilization mechanisms that will lead to improved stability and for providing guidelines for future device innovations. It should be noted that, as discussed above, there is an urgent need to distinguish between degradation resulting from beam damage during TEM characterization and degradation resulting from the experimental conditions, which is so far lacking in the reported literature.

Ion Migration in Halide Perovskite Devices

Ion migration is an important phenomenon in HPs, which has attracted significant attention in the field of PSCs and HP-based (opto)electronics. This is since Snaith et al.⁸⁷ proposed it as one possible reason for the anomalous photocurrent hysteresis in PSCs. It has been later related to another important issue of PSCs—degradation, as unintended loss of stoichiometry in HP absorber layers or harmful reaction of HPs with other PSC layers (charge-transporting layers, electrodes, etc.) that can possibly be caused by the migration of ions in HPs during the PSC operations.^{88–90} In addition, ion migration appears to be responsible for many other unique observations that have been made in HPs. These include switchable photovoltaic effects, “abnormal” dielectric properties, and memristive switching. Thus, there is an urgent need to have an in-depth understanding of the ion migration in HPs and/or PSCs, based on which the inhibition and manipulation of such behavior for better PSCs, as well as other HP-based (opto)electronic devices, can be made possible. Ion migration has been studied using a variety of methods such as nanoscale-resolution tunable pulsed infrared (IR) spectroscopy, photoluminescence (PL) spectroscopy, and electrochemical methods.⁹¹ However, direct reliable evidence for ion migration in HPs can only be provided by *operando* TEM studies.

Operando TEM has been successfully employed in revealing Li-ion conduction in battery materials, but in HPs, there is only limited information available in the literature. In this context, Jeangros et al.⁹² prepared a TEM sample by depositing TCO/PCBM(ETL)/MAPbI₃/spiro-OMeTAD(HTL)/Au on a Si wafer, and then prepared an FIB sample on a microelectromechanical chip for *operando* TEM experiment (left panel of Figure 9A). *In situ* characterization was performed using low beam-currents to reduce beam damage.⁹² Also, STEM characterization was performed with the beam blanked between image acquisitions.⁹² The right panel of Figure 9A shows a HAADF STEM image of the pristine device indicating that iodine has diffused into the HTL, which was assumed to be the result of the deposition process rather than the FIB sample preparation, as it was not dependent on the thickness of the FIB lamella. It is claimed that FIB sample preparation, in addition to exposure to air, has resulted in the degradation of MAPbI₃ to PbI₂.⁹² Changes in device morphology during the current density (J)-voltage (V) scan were recorded *in situ* in STEM mode. As seen in Figure 9B, by applying +6 V on the HTL/Au side of the device (J of 20 mA cm⁻², which is close to the short circuit, J_{SC} , of a typical PSC), nanoparticles started to appear at the HP interface with the HTL, and they continued to form upon prolonged biasing (arrows in Figure 9B).⁹² The HAADF intensity in the HTL region near the HP layer increased under biasing, suggesting ion migration of heavy

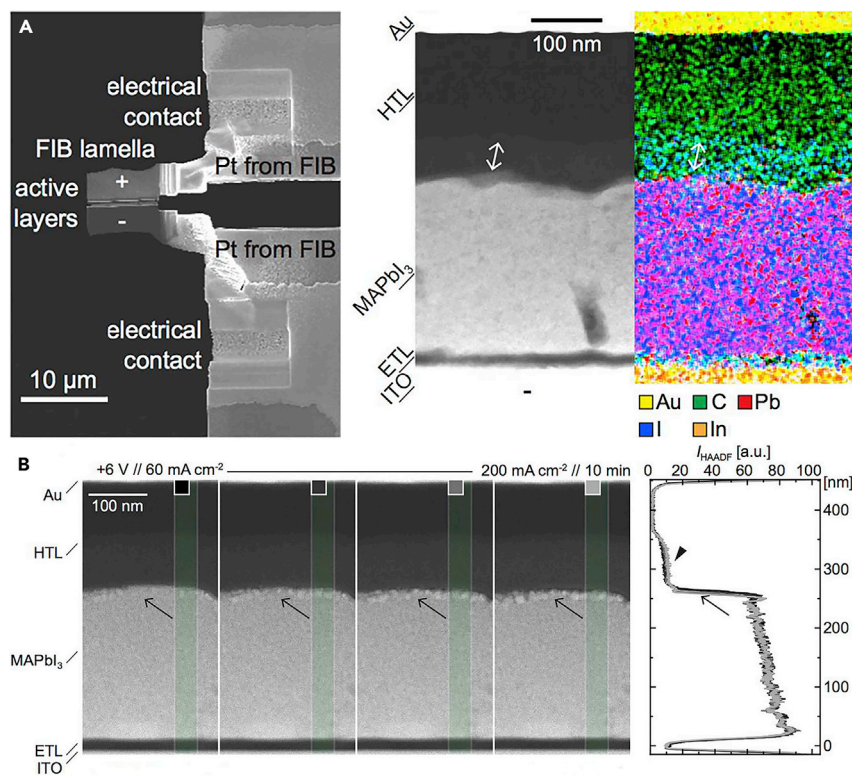


Figure 9. Ion Migration in PSCs under Electrical Bias

(A) SEM image of a FIB-prepared TEM lamella connected to a biasing chip for *in situ* TEM electrical measurements (left), and a HAADF STEM image in addition to the associated EDS map of the initial microstructure (right). The arrow indicates I in the HTL.

(B) HAADF STEM images showing microstructural changes when biasing for 10 min at 6 V with current density increasing from 60 to 200 mA cm⁻², in addition to the corresponding HAADF intensity profiles (right) which were integrated in the highlighted areas.

Adapted from Jeangros et al.⁹² with permission, the American Chemical Society.

elements, as marked by the arrowhead in the intensity profiles in Figure 9B, where in the sequence of images in Figure 9B the J through the cell increased from 60 to 200 mA cm⁻².⁹² However, when the V was reversed to -6 V (J - V breakdown condition) for 10 min, voids formed within the HP layer located at the interface with the ETL.⁹² At the same time, I-rich layer in the HTL did not evolve under this sequence. It should be taken into account that microstructural changes were also observed in regions that were not previously irradiated by the electron beam during biasing, confirming that biasing (rather than electron irradiation) is their source.⁹² In addition, electron irradiation caused PbI₂ nanoparticles formation upon current passing through the sample to be less visible, most likely due to amorphization and redispersion process.⁹² The type of nanoparticles was confirmed using EDS and HRTEM imaging.⁹² Pb-rich areas were also found by EDS in the spiro-OMeTAD layer. In addition, a lower I/Pb ratio was measured after biasing, indicating that some I (probably with some organic species) has volatilized. Within the detection limit of the EDS, the Au contact did not diffuse into the other layers.⁹² It is suggested that PbI₂ particles may have appeared along lines in which current was flowing and triggered degradation, whereas MAPbI₃ remained in certain regions.⁹² EDS, in addition to contrast changes in the HAADF STEM micrographs, confirmed that I⁻ has migrated into the positively charged HTL during electrical characterization.⁹² It is claimed that this process is reversed when the polarity is reversed.⁹² Based on these

observations, it is concluded that under forward-bias conditions, MAPbI₃ degradation occurs preferentially at the interface with the HTL, which is triggered by the migration of I⁻ into the HTL and the volatilization of I⁻ and organic species. This study involving *operando* TEM on HP devices not only provides critical insights into ion migration in MAPbI₃ HP devices but also draws important conclusions for future directions toward better devices. Parts of these results were confirmed by a recent study by Jung et al.,⁹³ who claim that oxygen ions migrate from the ETL to MAPbI₃ under forward biasing, which is associated with the structural changes in the form of amorphization of MAPbI₃ and PbI₂ formation. It should be considered that beam damage during TEM characterization (depending on the dose) and FIB sample preparation is expected to affect the degradation of HPs and HP based devices as was also discussed in the literature.^{41,56,92} Thus, there is a critical need to eliminate beam damage or access it when it is not possible to eliminate it, as was partly done in the reported literature.⁹²

OUTLOOK

In closing, TEM-based techniques are a set of powerful characterization tools that have not been widely applied to HP materials and devices, and they are expected to play a significant role in revealing the structural characteristics of HPs in the future. There is an urgent need to employ these tools to understand the nano-structures, micro-structures, morphological/phase evolution under environmental conditions, and ion-transport under electrical bias in HP materials and devices. The knowledge gained from this research will go a long way in answering some of the key questions in this field. These questions include, but are not limited to: What is the atomistic origin of the high optoelectronic properties and high photovoltaic performance of HPs? How do HPs crystallize from precursor phases? How do HPs degrade under atmospheric conditions? How can HPs be stabilized? What are the atomistic and micro-structural origins underlying the unconventional device phenomena (hysteresis, etc.)? Clarification of all of these key questions using TEM-based characterization is likely to contribute to the development of more effective protocols for achieving more efficient and stable PSCs and (opto)electronic devices.

ACKNOWLEDGMENTS

Funding from the US National Science Foundation (OIA-1538893), the US Office Naval Research (N00014-17-1-2232), and the Brown University Hibbitt Postdoctoral Fellowship (H.S.) is gratefully acknowledged. We thank Drs. A.R. Krause, A.L. Vasiliev, W. Wu, D. Zakharov, and L. Zhang for fruitful discussions.

DECLARATION OF INTERESTS

The authors declare no competing interests.

REFERENCES

1. Kojima, A., Teshima, K., Shirai, Y., and Miyasaka, T. (2009). Organometal halide perovskites as visible-light sensitizers for photovoltaic cells. *J. Am. Chem. Soc.* *131*, 6050–6051.
2. Snaith, H.J. (2018). Present status and future prospects of perovskite photovoltaics. *Nat. Mater.* *17*, 372–376.
3. Lee, M.M., Teuscher, J., Miyasaka, T., Murakami, T.N., and Snaith, H.J. (2012). Efficient hybrid solar cells based on meso-superstructured organometal halide perovskites. *Science* *338*, 643–647.
4. Kim, H.S., Lee, C.R., Im, J.H., Lee, K.B., Moehl, T., Marchioro, A., Moon, S.J., Humphry-Baker, R., Yum, J.H., Moser, J.E., et al. (2012). Lead iodide perovskite sensitized all-solid-state submicron thin film mesoscopic solar cell with efficiency exceeding 9%. *Sci. Rep.* *2*, 591.
5. Liu, M., Johnston, M.B., and Snaith, H.J. (2013). Efficient planar heterojunction perovskite solar cells by vapour deposition. *Nature* *501*, 395–398.
6. Seok, S.I., Grätzel, M., and Park, N.G. (2018). Methodologies toward highly efficient perovskite solar cells. *Small* *14*, <https://doi.org/10.1002/smll.201704177>.
7. NREL, Best Research-Cell Efficiencies, 2018, <https://www.nrel.gov/pv/assets/pdfs/pv-efficiency-chart.20181221.pdf>.
8. Rong, Y., Hu, Y., Mei, A., Tan, H., Saidaminov, M.I., Seok, S.I., McGehee, M.D., Sargent, E.H., and Han, H. (2018). Challenges for commercializing perovskite solar cells. *Science* *361*, eaat8235. <https://doi.org/10.1126/science.aat8235>.

9. Correa-Baena, J.P., Saliba, M., Buonassisi, T., Grätzel, M., Abate, A., Tress, W., and Hagfeldt, A. (2017). Promises and challenges of perovskite solar cells. *Science* **358**, 739–744.
10. Stoumpos, C.C., Cao, D.H., Clark, D.J., Young, J., Rondinelli, J.M., Jang, J.I., Hupp, J.T., and Kanatzidis, M.G. (2016). Ruddlesden–Popper hybrid lead iodide perovskite 2D homologous semiconductors. *Chem. Mater.* **28**, 2852–2867.
11. Ju, M.G., Dai, J., Ma, L., Zhou, Y., and Zeng, X.C. (2018). Zero-dimensional organic–inorganic perovskite variant: transition between molecular and solid crystal. *J. Am. Chem. Soc.* **140**, 10456–10463.
12. Yusoff, A.R.b.M., and Nazeeruddin, M.K. (2018). Low-Dimensional perovskites: From synthesis to stability in perovskite solar cells. *Adv. Energy Mater.* **8**, 1702073.
13. Mao, L., Ke, W., Pedesseau, L., Wu, Y., Katan, C., Even, J., Wasielewski, M.R., Stoumpos, C.C., and Kanatzidis, M.G. (2018). Hybrid Dion–Jacobson 2D lead iodide perovskites. *J. Am. Chem. Soc.* **140**, 3775–3783.
14. Williams, D.B., and Carter, C.B. (2009). *Transmission Electron Microscopy* (Springer).
15. Egerton, R.F. (1996). *Electron Energy-Loss Spectroscopy in the Electron Microscope* (Plenum Press).
16. Brandon, D.G., and Kaplan, W.D. (1999). *Microstructural Characterization of Materials* (Wiley).
17. Lentzen, M., Jahnen, B., Jia, C.L., Thust, A., Tillmann, K., and Urban, K. (2002). High-resolution imaging with an aberration-corrected transmission electron microscope. *Ultramicroscopy* **92**, 233–242.
18. Urban, K.W. (2008). Studying atomic structures by aberration-corrected transmission electron microscopy. *Science* **321**, 506–510.
19. Tillmann, K., Houben, L., Thust, A., and Urban, K. (2006). Spherical-aberration correction in tandem with the restoration of the exit-plane wavefunction: synergetic tools for the imaging of lattice imperfections in crystalline solids at atomic resolution. *J. Mater. Sci.* **41**, 4420–4433.
20. Allen, L.J., McBride, W., O’Leary, N.L., and Oxley, M.P. (2004). Exit-wave reconstruction at atomic resolution. *Ultramicroscopy* **100**, 91–104.
21. Kirkland, A.I., and Meyer, R.R. (2004). “Indirect” high-resolution transmission electron microscopy: aberration measurement and wavefunction reconstruction. *Microsc. Microanal.* **10**, 401–413.
22. Haigh, S.J., Sawada, H., Takayanagi, K., and Kirkland, A.I. (2010). Exceeding conventional resolution limits in high-resolution transmission electron microscopy using tilted illumination and exit-wave restoration. *Microsc. Microanal.* **16**, 409–415.
23. Haider, M., Hartel, P., Müller, H., Uhlemann, S., and Zach, J. (2010). Information transfer in a TEM corrected for spherical and chromatic aberration. *Microsc. Microanal.* **16**, 393–408.
24. Barthel, J., Houben, L., and Tillmann, K. (2015). FEI Titan G3. In *Pico*, pp. 50–300, Large-Scale. J. and Res. Facilities **1**, A34.
25. Buxton, B.F., Eades, J.A., Steeds, J.W., and Rackham, G.M. (1976). The symmetry of electron diffraction zone axis patterns. *Philosophical Transactions of the Royal Society A: Mathematical, Physical and Engineering Sciences* **281**, 171–194.
26. Egerton, R.F. (2009). Electron energy-loss spectroscopy in the TEM. *Rep. Prog. Phys.* **72**, 016502. <https://doi.org/10.1088/0034-4885/72/1/016502>.
27. Kraxner, J., Schäfer, M., Röschel, O., Kothleitner, G., Haberfehlner, G., Paller, M., and Grogger, W. (2017). Quantitative EDXS: influence of geometry on a four detector system. *Ultramicroscopy* **172**, 30–39.
28. Epicier, T., Aouine, M., Cadete Santos Aires, F.J., Massin, L., and Gélin, P. (2018). Experimental evidence for the existence of an iridium sesquioxide metastable phase during ETEM studies of methane steam reforming on an Ir/Ce_{0.9}Gd_{0.9}O_{2-x} catalyst. *Microsc. Microanal.* **24**, 1648–1649.
29. Gong, C., Robertson, A.W., He, K., Lee, G.D., Yoon, E., Allen, C.S., Kirkland, A.I., and Warner, J.H. (2015). Thermally induced dynamics of dislocations in graphene at atomic resolution. *ACS Nano* **9**, 10066–10075.
30. Almeida, T.P., Muxworthy, A.R., Kovács, A., Williams, W., Brown, P.D., and Dunin-Borkowski, R.E. (2016). Direct visualization of the thermomagnetic behavior of pseudo-single-domain magnetite particles. *Sci. Adv.* **2**, e1501801.
31. Jinschek, J.R. (2014). Advances in the environmental transmission electron microscope (ETEM) for nanoscale *in situ* studies of gas–solid interactions. *Chem. Commun.* **50**, 2696–2706.
32. Egerton, R.F., Li, P., and Malac, M. (2004). Radiation damage in the TEM and SEM. *Micron* **35**, 399–409.
33. Yoshida, K., and Sasaki, Y. (2013). Optimal accelerating voltage for HRTEM imaging of zeolite. *Microscopy* **62**, 369–375.
34. Clough, R.N., Moldovan, G., and Kirkland, A.I. (2014). Direct detectors for electron microscopy. *J. Phys. Conf. Ser.* **522**, 012046. <https://doi.org/10.1088/1742-6596/522/1/012046>.
35. Stach, E.A., Zakharov, D., Rivas, R.D., Longo, P., Lent, M., Gubbens, A., and Czarnek, C. (2013). Exploiting a direct detection camera for *in situ* microscopy. *Microsc. Microanal.* **19**, 392–393.
36. Huang, C., Borisenko, K.B., and Kirkland, A.I. (2014). Exit wave reconstruction of radiation-sensitive materials from low-dose data. *J. Phys.: Conf. Ser.* **522**, 012052. <https://doi.org/10.1088/1742-6596/522/1/012052>.
37. Chen, T., Foley, B.J., Ipek, B., Tyagi, M., Copley, J.R.D., Brown, C.M., Choi, J.J., and Lee, S.H. (2015). Rotational dynamics of organic cations in the CH₃NH₃PbI₃ perovskite. *Phys. Chem. Chem. Phys.* **17**, 31278–31286.
38. Leguy, A.M.A., Frost, J.M., McMahon, A.P., Sakai, V.G., Kockelmann, W., Law, C., Li, X., Foglia, F., Walsh, A., O’Regan, B.C., et al. (2015). The dynamics of methylammonium ions in hybrid organic–inorganic perovskite solar cells. *Nat. Comm.* **6**, 7124.
39. Wu, T., Collins, L., Zhang, J., Lin, P.Y., Ahmadi, M., Jesse, S., and Hu, B. (2017). Photoinduced bulk polarization and its effects on photovoltaic actions in perovskite solar cells. *ACS Nano* **11**, 11542–11549.
40. Dang, Z., Shamsi, J., Akkerman, Q.A., Imran, M., Bertoni, G., Brescia, R., and Manna, L. (2017). Low-temperature electron beam-induced transformations of cesium lead halide perovskite nanocrystals. *ACS Omega* **2**, 5660–5665.
41. Zhang, D., Zhu, Y., Liu, L., Ying, X., Hsiung, C.E., Sougrat, R., Li, K., and Han, Y. (2018). Atomic-resolution transmission electron microscopy of electron beam-sensitive crystalline materials. *Science* **359**, 675–679.
42. Kutes, Y., Ye, L., Zhou, Y., Pang, S., Huey, B.D., and Padture, N.P. (2014). Direct observation of ferroelectric domains in solution-processed CH₃NH₃PbI₃ perovskite thin films. *J. Phys. Chem. Lett.* **5**, 3335–3339.
43. Rakita, Y., Bar-Elli, O., Meirzadeh, E., Kaslasi, H., Peleg, Y., Hodes, G., Lubomirsky, I., Oron, D., Ehre, D., and Cahen, D. (2017). Tetragonal CH₃NH₃PbI₃ is ferroelectric. *Proc. Natl. Acad. Sci. USA* **114**, E5504–E5512.
44. Fan, Z., Xiao, J., Sun, K., Chen, L., Hu, Y., Ouyang, J., Ong, K.P., Zeng, K., and Wang, J. (2015). Ferroelectricity of CH₃NH₃PbI₃ perovskite. *J. Phys. Chem. Lett.* **6**, 1155–1161.
45. Yu, Y., Zhang, D., Kisielowski, C., Dou, L., Kornienko, N., Bekenstein, Y., Wong, A.B., Alivisatos, A.P., and Yang, P. (2016). Atomic resolution imaging of halide perovskites. *Nano Lett.* **16**, 7530–7535.
46. Chen, F.-R., Van Dyck, D., and Kisielowski, C. (2016). In-line three-dimensional holography of nanocrystalline objects at atomic resolution. *Nat. Comm.* **7**, 10603.
47. Koch, C.T. (2014). Towards full-resolution inline electron holography. *Micron* **63**, 69–75.
48. Kim, T.W., Uchida, S., Matsushita, T., Cojocar, L., Jono, R., Kimura, K., Matsubara, D., Shirai, M., Ito, K., Matsumoto, H., et al. (2018). Self-organized superlattice and phase coexistence inside thin film organometal halide perovskite. *Adv. Mater.* **30**, 1705230. <https://doi.org/10.1002/adma.201705230>.
49. Tae Woong, K., Tomonori, M., Satoshi, U., Takashi, K., and Hiroshi, S. (2018). Quantitative fraction analysis of coexisting phases in a polycrystalline CH₃NH₃PbI₃ perovskite. *Appl. Phys. Exp.* **11**.
50. Dar, M.I., Arora, N., Gao, P., Ahmad, S., Grätzel, M., and Nazeeruddin, M.K. (2014). Investigation regarding the role of chloride in organic-inorganic halide perovskites obtained from chloride containing precursors. *Nano Lett.* **14**, 6991–6996.
51. Reis, R.d., Yang, H., Ophus, C., Ercius, P., Bizarri, G., Perrodin, D., Shalapska, T., Bourret, E., Ciston, J., and Dahmen, U. (2018). Determination of the structural phase and

- octahedral rotation angle in halide perovskites. *Appl. Phys. Lett.* **112**, 071901.
52. Chen, Y., Sun, Y., Peng, J., Tang, J., Zheng, K., and Liang, Z. (2018). 2D Ruddlesden–Popper perovskites for optoelectronics. *Adv. Mater.* **30**, 1703487. <https://doi.org/10.1002/adma.201703487>.
 53. Yu, Y., Zhang, D., and Yang, P. (2017). Ruddlesden–Popper phase in two-dimensional inorganic halide perovskites: a plausible model and the supporting observations. *Nano Lett.* **17**, 5489–5494.
 54. Cowley, J.M. (1995). *Diffraction Physics* (Elsevier).
 55. Stadelmann, P.A. (1987). EMS — a software package for electron-diffraction analysis and HREM image simulation in materials science. *Ultramicroscopy* **21**, 131–145.
 56. Rothmann, M.U., Li, W., Zhu, Y., Liu, A., Ku, Z., Bach, U., Etheridge, J., and Cheng, Y.B. (2018). Structural and chemical changes to $\text{CH}_3\text{NH}_3\text{PbI}_3$ induced by electron and gallium ion beams. *Adv. Mater.* **30**, e1800629.
 57. Xiao, Z., Zhao, L., Tran, N.L., Lin, Y.L., Silver, S.H., Kerner, R.A., Yao, N., Kahn, A., Scholes, G.D., and Rand, B.P. (2017). Mixed-halide perovskites with stabilized bandgaps. *Nano Lett.* **17**, 6863–6869.
 58. Bekenstein, Y., Dahl, J.C., Huang, J., Osowiecki, W.T., Swabeck, J.K., Chan, E.M., Yang, P., and Alivisatos, A.P. (2018). The making and breaking of lead-free double perovskite nanocrystals of cesium silver–bismuth halide compositions. *Nano Lett.* **18**, 3502–3508.
 59. Saylor, D.M., El Dasher, B., Sano, T., and Rohrer, G.S. (2004). Distribution of grain boundaries in SrTiO_3 as a function of five macroscopic parameters. *J. Am. Ceram. Soc.* **87**, 670–676.
 60. Saylor, D.M., Morawiec, A., and Rohrer, G.S. (2003). Distribution of grain boundaries in magnesia as a function of five macroscopic parameters. *Acta Mater.* **51**, 3663–3674.
 61. Durose, K., and Russell, G.J. (1990). Twinning in CdTe . *J. Cryst. Growth* **101**, 246–250.
 62. Rothmann, M.U., Li, W., Zhu, Y., Bach, U., Spiccia, L., Etheridge, J., and Cheng, Y.B. (2017). Direct observation of intrinsic twin domains in tetragonal $\text{CH}_3\text{NH}_3\text{PbI}_3$. *Nat. Comm.* **8**, 14547.
 63. Li, W., Yadavalli, S.K., Lizarazo-Ferro, D., Chen, M., Zhou, Y., Padture, N.P., and Zia, R. (2018). Sub-grain special boundaries in halide perovskite thin films restrict carrier diffusion. *ACS Energy Lett.* **3**, 2669–2670.
 64. Zong, Y., Zhou, Y., Zhang, Y., Li, Z., Zhang, L., Ju, M.G., Chen, M., Pang, S., Zeng, X.C., and Padture, N.P. (2018). Continuous grain-boundary functionalization for high-efficiency perovskite solar cells with exceptional stability. *Chem* **4**, 1404–1415.
 65. Zhou, Y., Vasiliev, A.L., Wu, W., Yang, M., Pang, S., Zhu, K., and Padture, N.P. (2015). Crystal morphologies of organolead trihalide in mesoscopic/planar perovskite solar cells. *J. Phys. Chem. Lett.* **6**, 2292–2297.
 66. Yang, B., Dyck, O., Poplawsky, J., Keum, J., Puzetzy, A., Das, S., Ivanov, I., Rouleau, C., Duscher, G., Geoghegan, D., et al. (2015). Perovskite solar cells with near 100% internal quantum efficiency based on large single crystalline grains and vertical bulk heterojunctions. *J. Am. Chem. Soc.* **137**, 9210–9213.
 67. Shao, Y., Xiao, Z., Bi, C., Yuan, Y., and Huang, J. (2014). Origin and elimination of photocurrent hysteresis by fullerene passivation in $\text{CH}_3\text{NH}_3\text{PbI}_3$ planar heterojunction solar cells. *Nat. Comm.* **5**, 5784.
 68. Nanova, D., Kast, A.K., Pfannmöller, M., Müller, C., Veith, L., Wacker, I., Agari, M., Hermes, W., Erk, P., Kowalsky, W., et al. (2014). Unraveling the nanoscale morphologies of mesoporous perovskite solar cells and their correlation to device performance. *Nano Lett.* **14**, 2735–2740.
 69. Pfannmöller, M., Flügge, H., Benner, G., Wacker, I., Sommer, C., Hanselmann, M., Schmale, S., Schmidt, H., Hamprecht, F.A., Rabe, T., et al. (2011). Visualizing a homogeneous blend in bulk heterojunction polymer solar cells by analytical electron microscopy. *Nano Lett.* **11**, 3099–3107.
 70. Dunlap-Shohl, W.A., Zhou, Y., Padture, N.P., and Mitzi, D.B. (2018). Synthetic approaches for halide perovskite thin films. *Chem. Revolution*. <https://doi.org/10.1021/acs.chemrev.8b00318>.
 71. Zhou, Y., Game, O.S., Pang, S., and Padture, N.P. (2015). Microstructures of organometal trihalide perovskites for solar cells: their evolution from solutions and characterization. *J. Phys. Chem. Lett.* **6**, 4827–4839.
 72. Qin, F., Wang, Z., and Wang, Z.L. (2016). Anomalous growth and coalescence dynamics of hybrid perovskite nanoparticles observed by liquid-cell transmission electron microscopy. *ACS Nano* **10**, 9787–9793.
 73. Aguiar, J.A., Wozny, S., Holesinger, T.G., Aoki, T., Patel, M.K., Yang, M., Berry, J.J., Al-Jassim, M., Zhou, W., and Zhu, K. (2016). *In situ* investigation of the formation and metastability of formamidinium lead tri-iodide perovskite solar cells. *Energy Environ. Sci.* **9**, 2372–2382.
 74. Wang, Q., Chen, B., Liu, Y., Deng, Y., Bai, Y., Dong, Q., and Huang, J. (2017). Scaling behavior of moisture-induced grain degradation in polycrystalline hybrid perovskite thin films. *Energy Environ. Sci.* **10**, 516–522.
 75. Ji, F., Pang, S., Zhang, L., Zong, Y., Cui, G., Padture, N.P., and Zhou, Y. (2017). Simultaneous evolution of uniaxially oriented grains and ultralow-density grain-boundary network in $\text{CH}_3\text{NH}_3\text{PbI}_3$ perovskite thin films mediated by precursor phase metastability. *ACS Energy Lett.* **2**, 2727–2733.
 76. Kim, T.W., Shibayama, N., Cojocar, L., Uchida, S., Kondo, T., and Segawa, H. (2018). Real-Time *in situ* observation of microstructural change in organometal halide perovskite induced by thermal degradation. *Adv. Funct. Mater.* **28**, <https://doi.org/10.1002/adfm.201804039>.
 77. Chen, S., Zhang, X., Zhao, J., Zhang, Y., Kong, G., Li, Q., Li, N., Yu, Y., Xu, N., Zhang, J., et al. (2018). Atomic scale insights into structure instability and decomposition pathway of methylammonium lead iodide perovskite. *Nat. Commun.* **9**, 4807.
 78. Aguiar, J.A., Wozny, S., Alkurd, N.R., Yang, M., Kovarik, L., Holesinger, T.G., Al-Jassim, M., Zhu, K., Zhou, W., and Berry, J.J. (2016). Effect of water vapor, temperature, and rapid annealing on formamidinium lead triiodide perovskite crystallization. *ACS Energy Lett.* **1**, 155–161.
 79. Fan, Z., Xiao, H., Wang, Y., Zhao, Z., Lin, Z., Cheng, H.-C., Lee, S.-J., Wang, G., Feng, Z., Goddard, W.A., et al. (2017). Layer-by-layer degradation of methylammonium lead tri-iodide perovskite microplates. *Joule* **1**, 548–562.
 80. Patel, J.B., Milot, R.L., Wright, A.D., Herz, L.M., and Johnston, M.B. (2016). Formation dynamics of $\text{CH}_3\text{NH}_3\text{PbI}_3$ perovskite following two-step layer deposition. *J. Phys. Chem. Lett.* **7**, 96–102.
 81. Dang, Z., Shamsi, J., Palazon, F., Imran, M., Akkerman, Q.A., Park, S., Bertoni, G., Prato, M., Brescia, R., and Manna, L. (2017). *In situ* transmission electron microscopy study of electron beam-induced transformations in colloidal cesium lead halide perovskite nanocrystals. *ACS Nano* **11**, 2124–2132.
 82. Chen, X., and Wang, Z. (2019). Investigating Chemical and structural instabilities of lead halide perovskite induced by electron beam irradiation. *Micron* **116**, 73–79.
 83. Saliba, M., Matsui, T., Seo, J.-Y., Domanski, K., Correa-Baena, J.-P., Nazzeeruddin, M.K., Zakeeruddin, S.M., Tress, W., Abate, A., Hagfeldt, A., et al. (2016). Cesium-containing triple cation perovskite solar cells: improved stability, reproducibility and high efficiency. *Energy Environ. Sci.* **9**, 1989–1997.
 84. Saliba, M., Matsui, T., Domanski, K., Seo, J.-Y., Ummadisingu, A., Zakeeruddin, S.M., Correa-Baena, J.-P., Tress, W.R., Abate, A., Hagfeldt, A., et al. (2016). Incorporation of rubidium cations into perovskite solar cells improves photovoltaic performance. *Science* **354**, 206–209.
 85. Yang, B., Dyck, O., Ming, W., Du, M.-H., Das, S., Rouleau, C.M., Duscher, G., Geoghegan, D.B., and Xiao, K. (2016). Observation of nanoscale morphological and structural degradation in perovskite solar cells by *in situ* TEM. *ACS Appl. Mater. Interfaces* **8**, 32333–32340.
 86. Divitini, G., Cacovich, S., Matteocci, F., Cinà, L., Di Carlo, A., and Ducati, C. (2016). *In situ* observation of heat-induced degradation of perovskite solar cells. *Nat. Energy* **1**, 15012.
 87. Snaith, H.J., Abate, A., Ball, J.M., Eperon, G.E., Leijtens, T., Noel, N.K., Stranks, S.D., Wang, J.T.-W., Wojciechowski, K., and Zhang, W. (2014). Anomalous hysteresis in perovskite solar cells. *J. Phys. Chem. Lett.* **5**, 1511–1515.
 88. Li, Z., Xiao, C., Yang, Y., Harvey, S.P., Kim, D.H., Christians, J.A., Yang, M., Schulz, P., Nanayakkara, S.U., Jiang, C.S., et al. (2017). Extrinsic ion migration in perovskite solar cells. *Energy Environ. Sci.* **10**, 1234–1242.
 89. Miyano, K., Yanagida, M., Tripathi, N., and Shirai, Y. (2016). Hysteresis, stability, and ion migration in lead halide perovskite

- photovoltaics. *J. Phys. Chem. Lett.* **7**, 2240–2245.
90. Li, J., Dong, Q., Li, N., and Wang, L. (2017). Direct evidence of ion diffusion for the silver-electrode-induced thermal degradation of inverted perovskite solar cells. *Adv. Energy Mater.* **7**, 1602922. <https://doi.org/10.1002/aenm.201602922>.
91. Yuan, Y., and Huang, J. (2016). Ion migration in organometal trihalide perovskite and its impact on photovoltaic efficiency and stability. *Acc. Chem. Res.* **49**, 286–293.
92. Jeangros, Q., Duchamp, M., Werner, J., Kruth, M., Dunin-Borkowski, R.E., Niesen, B., Ballif, C., and Hessler-Wyser, A. (2016). *In situ* TEM analysis of organic–inorganic metal-halide perovskite solar cells under electrical bias. *Nano Lett.* **16**, 7013–7018.
93. Jung, H.J., Kim, D., Kim, S., Park, J., Dravid, V.P., and Shin, B. (2018). Stability of halide perovskite solar cell devices: *in situ* observation of oxygen diffusion under biasing. *Adv. Mater.* **30**, 1802769. <https://doi.org/10.1002/adma.201802769>.